Advances in Water Resources 116 (2018) 208–218

Contents lists available at ScienceDirect

Advances in Water Resources

journal homepage: www.elsevier.com/locate/advwatres

Pore scale study of multiphase multicomponent reactive transport during CO_2 dissolution trapping

Li Chen[a,*], Mengyi Wang[a], Qinjun Kang[b], Wenquan Tao[a]

[a] Key Laboratory of Thermo-Fluid Science and Engineering of MOE, School of Energy and Power Engineering, Xi'an Jiaotong University, Xi'an, Shaanxi 710049, China
[b] Computational Earth Science, EES-16, Earth and Environmental Sciences Division, Los Alamos National Laboratory, Los Alamos, NM 87544, USA

ARTICLE INFO

Keyword:
CO_2 sequestration
Solubility trapping
Multiphase flow
Reactive transport
Porous media
Lattice Boltzmann method

ABSTRACT

Solubility trapping is crucial for permanent CO_2 sequestration in deep saline aquifers. For the first time, a pore-scale numerical method is developed to investigate coupled $scCO_2$-water two-phase flow, multicomponent (CO_2(aq), H^+, HCO_3^-, CO_3^{2-} and OH^-) mass transport, heterogeneous interfacial dissolution reaction, and homogeneous dissociation reactions. Pore-scale details of evolutions of multiphase distributions and concentration fields are presented and discussed. Time evolutions of several variables including averaged CO_2(aq) concentration, $scCO_2$ saturation, and pH value are analyzed. Specific interfacial length, an important variable which cannot be determined but is required by continuum models, is investigated in detail. Mass transport coefficient or efficient dissolution rate is also evaluated. The pore-scale results show strong non-equilibrium characteristics during solubility trapping due to non-uniform distributions of multiphase as well as slow mass transport process. Complicated coupling mechanisms between multiphase flow, mass transport and chemical reactions are also revealed. Finally, effects of wettability are also studied. The pore-scale studies provide deep understanding of non-linear non-equilibrium multiple physicochemical processes during CO_2 solubility trapping processes, and also allow to quantitatively predict some important empirical relationships, such as saturation-interfacial surface area, for continuum models.

1. Background

Multiphase reactive transport processes in porous media are widely encountered in scientific problems and engineering processes. Such processes are very complex due to multiple processes, dynamic phase interface evolution, and strong interaction between different processes. Taking carbon dioxide (CO_2) geo-sequestration, which is the topic of the present study, as an example. CO_2 geo-sequestration is currently considered as a method to limit greenhouse gas emissions into the atmosphere. During the sequestration, supercritical CO_2 (herein referred as $scCO_2$) is injected into deep saline aquifers or hydrocarbon reservoirs. Typically there are four principal trapping mechanisms of CO_2 at different time scales (IPCC, 2005): structural trapping, capillary trapping, dissolution trapping and mineral trapping. The lower density of $scCO_2$ compared with brine results in upward buoyant migration of $scCO_2$, which is prevented by low permeability caprocks, and such process is termed structural trapping. Capillary trapping is a process in which microscale $scCO_2$ bubbles (ganglia) are immobilized by capillary force inside the complex porous structures of the storage rock. $scCO_2$ dissolves into the surrounding brine through the brine-$scCO_2$ interface, and decreases the brine pH, resulting in dissolution trapping. Chemical reactions between the ions dissolved and formation minerals lead to the permanent mineral trapping. From the above description, it can be found that multiple physicochemical processes are involved including $scCO_2$-brine two phase flow, multicomponent transport, $scCO_2$ dissolution, and mineral dissolution and precipitation.

While there has been much analysis and observation of macroscale phenomena related to the above processes, the underlying details of the small-scale processes that dominate system behavior, such as phase interface evolution, interfacial mass transport and chemical reactions, pore-scale species concentration distribution, etc., remain unrevealed. Understanding the meso/microscopic phenomena and the interaction between different processes is critical to achieving a better prediction of the related systems and to improving sequestration efficiency. Changes in pore-scale multiphase flow and reactive transport processes sometimes lead to significant variation of macroscopic phenomena. To date, great efforts have been devoted to understanding mechanisms of pore-scale reactive transport processes related to different trapping mechanisms. Capillary trapping can account for 10%–90% of the total injected volume of CO_2 (Iglauer et al., 2011). During capillary trapping, $scCO_2$ saturation and distribution in porous rocks are affected by lots of factors such as pressure, temperature, brine salinity, pore size distribution,

* Corresponding author.
E-mail address: lichennht08@mail.xjtu.edu.cn (L. Chen).

https://doi.org/10.1016/j.advwatres.2018.02.018
Received 19 September 2017; Received in revised form 18 February 2018; Accepted 25 February 2018
Available online 26 April 2018

wettability, etc. Experiment techniques such as X-ray micro-tomography have been developed to visualize pore-scale $scCO_2$ distributions under different thermo-physical conditions (Andrew et al., 2014; Chaudhary et al., 2013). To name only a few, Andrew et al. (2014) adopted X-ray to image $scCO_2$ in carbonates and sandstones under typical storage pressures and temperatures. It was found that the size distribution of residual ganglia obeys power law distributions. Besides, mineral trapping leads to permanent CO_2 sequestration. Luquot and Gouze (2009) experimentally studied the processes of $scCO_2$ flow-through limestone reservoir samples. Different CO_2 pressure leads to quite different rock dissolution patterns driven by transport-controlled or reaction-controlled mass transfer. Power-law relationship between porosity and permeability during dissolution processes was obtained. With relatively low CO_2 pressure, decrease of porosity was observed due to mineral precipitation (Luquot and Gouze, 2009).

Chemical reactions play significant roles on $scCO_2$ dissolutions, mineral dissolution and precipitation. In the literature, mineral dissolution and precipitation reactions have been extensively studied at the pore-scale, both experimentally and numerically. Different mineral dissolution processes including face-dissolution, uniform dissolution and channel dissolution (wormhole phenomena) have been identified under different flow, mass transfer and reaction rates (Luquot and Gouze, 2009; Kang et al., 2002; Tartakovsky et al., 2007; Noiriel et al., 2009; Szymczak and Ladd, 2009; Kang et al., 2010; Yoon et al., 2012). For the dissolution trapping, studies related to pore-scale $scCO_2$ dissolution processes are scarce (Soltanian et al., 2017), mainly for two reasons. On the one hand, $scCO_2$ dissolution has long been treated as an equilibrium process. Thus immiscible experiments, in which $scCO_2$ and water are equilibrated prior to injection, are usually performed in the literature focusing on multiphase flow processes without $scCO_2$ dissolution (Pentland et al., 2011; Andrew et al., 2013). However, due to non-uniform $scCO_2$ distribution and limited mass transport rate, $scCO_2$ dissolution is actually a non-equilibrium process requiring a prolonged time to deplete $scCO_2$ (Paterson et al., 2013; Akbarabadi and Piri, 2013). On the other hand, during $scCO_2$ dissolution, multiple physicochemical processes are involved including phase interface evolution, fluid-fluid interfacial chemical reaction, multicomponent mass transport, and reactions at fluid-solid interface. It is really challenging for current experimental techniques to capture all the physical fields interested (velocity, concentration, phase interface, etc.) within limited space of porous media. To the best of our knowledge, until very recently there are a few experimental studies available in the literature (Buchgraber et al., 2012; Chang et al., 2016; Chang et al., 2017). These studies are benefited from advanced microfluidic techniques which allow direct observation of $scCO_2$-brine distribution and dissolution processes. Buchgraber et al. (2012) adopted 2D silicon micromodels represented Berea sandstone to investigate $scCO_2$ dissolution processes. Chang et al. (2016,2017) further performed comprehensive studies of $scCO_2$ dissolution under imbibition and drainage conditions. A set of $scCO_2$ dissolution experiments were performed in a heterogeneous 2D sandstone-analog micromodel at supercritical conditions. Based on the high resolution images of $scCO_2$-brine distribution and phase evolution, several $scCO_2$ dissolution types were identified depending on local pore structure and mass transport rate.

Multiphase flow reactive transport in brine-$scCO_2$-rock system depends on several parameters, such as pressure, temperature, flow rate, porosity, reactive surface area, tortuosity, wettability, etc. (Jun et al., 2013). The behavior of such coupled processes is unpredictable without the help of numerical modeling. Besides, compared with experimental studies, details of multiphase flow and reactive transport processes, especially the transport processes and species concentration distributions in different fluid phases, can be well captured by numerical modeling. However, due to the complex porous structures, multiple physicochemical processes, and strong interactions between different processes, it remains challenging to develop corresponding pore-scale numerical models. Such models should have the following abilities including capturing multiphase flow and distributions, taking into account both homogeneous and heterogeneous reactions, multicomponent mass transfer, and possible solid skeleton alteration. The aim of the present study is to develop an advanced pore-scale multiphase reactive transport model which can be applied to, but not limited to the reactive transport processes during $scCO_2$ dissolution process, and further to investigate the underlying details of $scCO_2$-water distribution and evolution, concentration fields and time evolutions of important parameters. To the best of our knowledge, this study is the first one for numerically studying at the pore-scale coupled multiphase flow and chemical reactions in porous rocks during $scCO_2$ sequestration.

2. Numerical method

With the improvement of computational resources, pore-scale modeling, in which the complicated structures of a porous medium are explicitly resolved, has become a critical technique for exploring microscopic multiple physicochemical processes and underlying mechanisms. Both “top-down” or “bottom-up” numerical methods have been adopted for pore-scale modeling (Chen et al., 2013a). Conventional CFD methods such as finite volume method (FVM), finite element method (FEM), and finite difference method (FDM), solve the Navier–Stokes equation (mass, momentum, energy and concentration, etc.) directly and thus belong to “top-down” methods. The main challenge encountered by such methods is grid generation of complex porous structures and boundary treatment at complicated phase boundary. Molecular dynamics (MD), which falls in the category of “bottom-up” method, requires unacceptable computation resources, thus limiting its application to problems of engineering interest. The lattice Boltzmann method (LBM, also a bottom-up method), which is a mesoscopic method occupying the middle ground between conventional CFD methods and MD, has developed into an alternative and promising numerical approach for simulating transport processes in recent years (Chen and Doolen, 1998; Zhang, 2011; Chen et al., 2014). Due to its kinetic intrinsic, the LBM has powerful capacity to treat complex boundaries and thus is particularly suitable for transport in porous media. At present, the LBM has been successfully adopted for investigating a variety of transport phenomena including porous flow, multiphase flow, heat transfer, chemical reaction, turbulent flow, slip flow, non-Newtonian flow and electrokinetic flow (Chen and Doolen, 1998; Zhang, 2011; Chen et al., 2014).

For the coupled multiphase flow and reactive transport processes studied in the present study, multiple sub-processes are involved, and thus the pore-scale numerical model developed must be able to handle the following major fundamental issues: to capture the deformable liquid-gas interfaces, to simulate mass transfer in the multiphase systems, and to treat both homogeneous and heterogeneous chemical reactions. There have been a few numerical studies about pore-scale multiphase reactive transport processes in porous media (Huber et al., 2011; Chen et al., 2013b, 2015a). In our previous studies, several LB models were selected and were delicately coupled to develop an advanced pore-scale model for coupled multiphase flow, single component transport, and reactive transport processes during nuclear waste storage (Chen et al., 2013b). Later, the above single-component multiphase pore-scale model was extended to multicomponent multiphase flow during shale gas exploitation (Chen et al., 2015a). In Ref. Chen et al. (2015a), the mass transport of each component was solved. This, however, is not necessary, because by writing chemical reactions in the canonical form components can be classified into primary and secondary components and only the total concentration of primary components is required to be solved (Kang et al., 2006). Note that in Ref. Kang et al. (2006) only single-phase reactive transport processes were studied. In this study, we further develop and improve our pore-scale multicomponent multiphase flow model (Chen et al., 2015a) based on such scheme to delineate the primary and secondary components. The numerical schemes and LB models are briefly introduced as follows.

2.1. Multiphase flow model

In the present study, the pseudopotential LB model proposed by Shan and Chen (herein referred to SC model) (Chen et al., 2014; Shan and Chen, 1993) is adopted for simulating $scCO_2$-brine two phase flow. Originally, velocity shifting scheme was employed for incorporating the external force into the SC model, which is criticized for leading to large spurious currents and low viscosity ratio (Shan and Chen, 1993). Later, the explicit forcing (EF) scheme is developed to induce the force directly in the discrete Boltzmann equations (Kupershtokh et al., 2009). Using the EF together with the multiple-relation time (MRT) collision term, the spurious current can be greatly reduced and the viscosity ratio can be greatly increased (Porter et al., 2012). The evolution equation of the density distribution function for kth component with MRT and EF schemes adopted is given by

$$f_\alpha^k(\mathbf{x}+c\mathbf{e}_\alpha\Delta t, t+\Delta t)-f_\alpha^k(\mathbf{x},t) = -\left(\mathbf{T}^{-1}\cdot\mathbf{M}^k\cdot\mathbf{T}\right)\left[f_\alpha^k(\mathbf{x},t)-f_\alpha^{\mathrm{eq},k}(\mathbf{x},t)\right]+\Delta t\left(\mathbf{T}^{-1}\cdot\left(\mathbf{I}-\frac{\mathbf{M}^k}{2}\right)\cdot\mathbf{T}\right)f_\alpha^{F,k}(\mathbf{x},t) \tag{1}$$

where f_α^k is the density distribution function at the lattice site $\mathbf{x}$ and time t, f^{eq} is the equilibrium distribution function, $c=\Delta x/\Delta t$ is the lattice speed with Δx and Δt are the lattice spacing and time step. The discrete velocities $\mathbf{e}_\alpha$ depend on the particular velocity model. D2Q9 lattice model is adopted for the present 2D study. The equilibrium distribution functions f^{eq} for kth component are as follows

$$f_\alpha^{eq,k}=\omega_\alpha\rho^k\left[1+\frac{3}{c^2}\left(\mathbf{e}_\alpha\cdot\mathbf{u}_k^{\mathrm{eq}}\right)+\frac{9}{2c^4}\left(\mathbf{e}_\alpha\cdot\mathbf{u}_k^{\mathrm{eq}}\right)^2-\frac{3}{2c^2}\left(\mathbf{u}_k^{\mathrm{eq}}\right)^2\right] \tag{2}$$

Matrix $\mathbf{T}$ in Eq. (1) is used to transfer distribution functions in the velocity space to the moment space. For 2D problem studied in this work, it is given by

$$\mathbf{T}=\begin{bmatrix}1,1,1,1,1,1,1,1,1\\-4,-1,-1,-1,-1,2,2,2,2\\4,-2,-2,-2,-2,1,1,1,1\\0,1,0,-1,0,1,-1,-1,1\\0,-2,0,2,0,1,-1,-1,1\\0,0,1,0,-1,1,1,-1,-1\\0,0,-2,0,2,1,1,-1,-1\\0,1,-1,1,-1,0,0,0,0\\0,0,0,0,0,1,-1,1,-1\end{bmatrix} \tag{3}$$

$\mathbf{T}^{-1}$ is the inverse matrix of $\mathbf{T}$. The diagonal relaxation matrix $\mathbf{M}$ is defined as

$$\mathbf{M}^k=\mathrm{diag}\left[s_c^k,s_e^k,s_\varepsilon^k,s_c^k,s_q^k,s_c^k,s_q^k,s_\upsilon^k,s_\upsilon^k\right] \tag{4}$$

s_c^k corresponds to the conserved moments and is set as unity in our simulations. s_e^k, s_ε^k and s_q^k correspond to non-conserved moments, and they are free parameters which can be adjusted to improve the accuracy and stability of the MRT model. Values of these free parameters are as follows in this study: $s_e^k=0.6$, $s_\varepsilon^k=1.5$ and $s_q^k=1.2$. s_υ^k is related to the viscosity of the kth component fluid

$$\upsilon^k=\frac{1}{3}\left(\frac{1}{s_\upsilon^k}-0.5\right)\frac{\Delta x^2}{\Delta t} \tag{5}$$

With the EF force scheme, the forcing term in Eq. (1) is defined as

$$f_\alpha^{F,k}=\frac{\mathbf{F}^k\cdot(\mathbf{e}_\alpha-\mathbf{u}^{\mathrm{eq}})}{\rho^k{c_s}^2}f_\alpha^{eq,k} \tag{6}$$

$\mathbf{u}^{\mathrm{eq}}$, the effective velocity, in Eq. (6) is calculated by

$$\mathbf{u}^{\mathrm{eq}}=\sum s_c^k\rho^k\mathbf{u}^k/\sum s_c^k\rho^k \tag{7}$$

which also equals $\mathbf{u}_k^{\mathrm{eq}}$ in Eq. (2). Density and velocity of each component are determined by

$$\rho^k=\sum f_\alpha^k,\ \rho^k\mathbf{u}^k=\sum f_\alpha^k\mathbf{e}_\alpha+\frac{\delta t}{2}\mathbf{F}^k \tag{8}$$

and the total density and physical velocity of the fluid mixture are calculated by

$$\rho=\sum\rho^k,\ \mathbf{u}=\sum\rho^k\mathbf{u}^k/\sum\rho^k \tag{9}$$

$\mathbf{F}^k$ in Eqs. (6) and (8) is the total force acting on kth component including fluid-fluid interaction force, fluid-solid interaction force and possible external body force such as gravity

$$\mathbf{F}^k=\mathbf{F}_f^k+\mathbf{F}_s^k+\mathbf{F}_e^k \tag{10}$$

The total fluid–fluid surface tension force acting on the particles of the kth component at lattice site $\mathbf{x}$ is defined as

$$\mathbf{F}_f^k=-\psi^k\left(\rho^k(\mathbf{x})\right)g_f\sum_{\mathbf{x}'}\sum_{\bar{k}}w(\mathbf{x}')\psi^{\bar{k}}\left(\rho^{\bar{k}}(\mathbf{x}')\right)(\mathbf{x}'-\mathbf{x}) \tag{11}$$

ψ is the effective mass or the pseudopotential, which is defined as $\psi^k(\rho^k)=1\text{-}\exp(\text{-}\rho^k)$ in our simulations. $g_f$controls the strength between fluids, and mixing between different components can be adjusted by changing g_f. $w(\mathbf{x}')$ are the weights. If only the interactions of four nearest neighbors with $|\mathbf{x}'-\mathbf{x}|^2=1$ and the four next-nearest neighbors $|\mathbf{x}'-\mathbf{x}|^2=2$ are considered, $w(1)=1/3$ and $w(2)=1/12$. The fluid-solid interaction force is introduced to describe the interaction between kth fluid and solid walls

$$\mathbf{F}_s^k=-\psi^k\left(\rho^k(\mathbf{x})\right)g_s\sum_{\mathbf{x}'}w(\mathbf{x}')S(\mathbf{x}')(\mathbf{x}'-\mathbf{x}) \tag{12}$$

where S is an indicator function and equals 0 and 1 for pore and solid, respectively. The coefficient g_s, which controls the strength between fluid and wall, is positive for non-wetting fluid and negative for wetting fluid. Different wettability (contact angle) can be obtained by adjusting g_s.

2.2. Multicomponent transport with chemical reactions

There are two kinds of reactions during species transport in porous media, namely the homogeneous reactions in the bulk fluid phase and the heterogeneous reactions at phase interface (Kang et al., 2006). The treatment of the two kinds of reactions in the LB framework are introduced as follows.

2.2.1. Homogeneous reactions

Homogeneous chemical reactions taking place in an aqueous fluid can be written in the following general form (Kang et al., 2006)

$$0\Leftrightarrow\sum_{k=1}^{N}\nu_{kr}A_k,\quad(r=1,\ ...,\ N_R) \tag{13}$$

where N is the total number of aqueous species, N_{R} is the number of reactions, A_k is kth species, and ν_{kr} is the stoichiometric coefficient. The above reactions can be written in the canonical form with all the species categorized into primary and secondary species (Kang et al., 2006)

$$\sum_{j=1}^{N_C}\nu_{ji}A_j\Leftrightarrow A_i\quad(r=1,\ ...,\ N_R) \tag{14}$$

where N_{C} and N_{R} are the number of the primary and secondary species, respectively. Instead of solving a LB concentration evolution equation for concentration distribution function g for each species, with some summation operations and introduction of the following physical variable (Kang et al., 2006)

$$\varphi_j=\sum_\alpha G_{\alpha j}=C_j+\sum_{i=1}^{N_R}\nu_{ji}C_i \tag{15}$$

where φ_j denotes the total concentration of the jth primary species. $G_{\alpha j}$ is the concentration distribution function of φ_j and is expressed as follows

$$G_{\alpha j}=g_{\alpha j}+\sum_{i=1}^{N_R}\nu_{ji}g_{\alpha i} \tag{16}$$

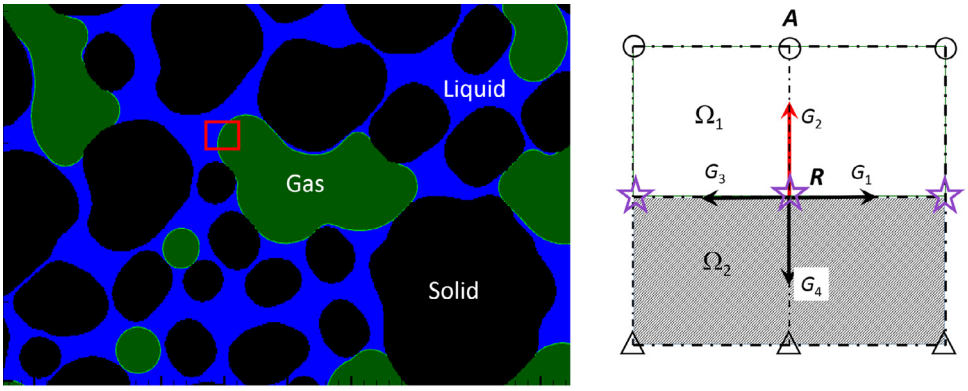

(a) Liquid-gas-solid three phase system (b) Schematic of interfacial boundary

Fig. 1. A gas-liquid-solid three phase system and the schematic of the interfacial boundary.

The LB evolution equation for G is given by (Kang et al., 2006)

$$G_{\alpha j}(\mathbf{x}+\mathbf{e}_\alpha\Delta_t, t+\Delta_t) = G_{\alpha j}(\mathbf{x},t) - \frac{G_{\alpha j}(\mathbf{x},t) - G^{eq}_{\alpha j}(\varphi_j,\mathbf{u})}{\tau_{aq}}, (j=1,...,N_C) \tag{17}$$

Eq. (17) can be proved to recover the advection-diffusion equation for φ_j. Assuming the homogeneous reactions are in instantaneous equilibrium, the following mass action equations can be obtained

$$C_i = (\gamma_i)^{-1} K_i \prod_{j=1}^{N_C} (\gamma_j C_j)^{\nu_{ji}} \tag{18}$$

where K_i is the equilibrium constant of the ith homogeneous reaction and γ_i is the activity of the ith secondary species.

During the simulation of species transport, Eq. (17) is first solved to obtain φ_j. Then Eq. (18) is substituted into Eq. (15), and Eq. (15) is solved using Newton Raphson iteration to obtain C_j. Finally, C_i is calculated using Eq. (18) with knownC_j. From Eqs. (13) to (18) it can be found that the number of LB concentration evolution equations required to be solved is reduced from $N_C + N_R$ to N_R, meaning higher efficiency of the numerical models especially for a system with many aqueous species. This allows us to improve our multicomponent multiphase flow pore-scale model in this work.

For 2D case in this study, D2Q5 lattice model is adopted to solve the mass transport (Chen et al., 2012). The equilibrium distribution function G^{eq} is given by

$$G^{eq} = C(a_i + 0.5\mathbf{e}_i\cdot\mathbf{u}),\ a_i = \begin{cases} J & i=0 \\ (1-J)/4 & i=1\sim 4 \end{cases} \tag{19}$$

The concentration and the diffusivity are obtained by $\varphi = \Sigma G$ and $D = (1-J)(\tau_q - 0.5)\Delta x^2/2\Delta t$, respectively. Weight factor J is set as 0.2.

2.2.2. Heterogeneous interfacial reaction treatment

For multiphase reactive transport processes in porous media, heterogeneous chemical reactions are possible to take place at any phase interface. Taking a gas-liquid-solid three phase system in Fig. 1(a) as an example, chemical reactions are likely to occur at liquid-solid, gas-solid, or liquid-gas interface, depending on specific circumstance studied. In our previous work, a general LB concentration boundary scheme was proposed (Chen et al., 2013b). Fig. 1(b) represents local computational mesh system of the phase interface in the red square of Fig. 1(a). If a species C is only allowed to transport in domain Ω_1 marked by circles (see Fig. 1(b)), then the distribution function G_2 is unknown for an interface node **R** between Ω_1 and Ω_2, the value of which should be assigned for subsequent streaming steps in the LB framework. Obviously, G_2 is higher than G_4 if species A is generated by the surface reaction, and vice versa. The macroscopic concentration boundary condition at the phase interface is expressed in the following general form (Zhang et al., 2012):

$$b_1\frac{\partial\varphi}{\partial\mathbf{n}} + b_2\varphi = b_3 \tag{20}$$

which is a general formula that can describe all the three types of boundary conditions: the Dirichlet boundary condition, with $b_1 = 0$ and $b_2 \neq 0$; the Neumann boundary condition, with $b_2 = 0$ and $b_1 \neq 0$; and a mixed boundary condition, with $b_1 \neq 0$ and $b_2 \neq 0$.

The first order moment of the distribution functions is as follows:

$$\sum G_\alpha \mathbf{e}_\alpha = \varphi\mathbf{u} - D\nabla\varphi \tag{21}$$

Eqs. (20) and (21) together constitute the general LB concentration boundary condition (Chen et al., 2013b). φ at the boundary is first solved using Eq. (20)

$$b_1\frac{\varphi_A - \varphi_R}{\Delta y} + b_2\varphi_R = b_3 \tag{22}$$

with the first term in (20) discretized by first order difference scheme, and of course higher order difference scheme can be adopted. With φ_R known, Eq. (21) is then used to solve the only unknown distribution function, which is G_2 in Fig. 1(b). The above LB boundary condition is a general one no matter the boundary is moving or not, or it involves chemical reaction or not (Chen et al., 2013b).

3. Physicochemical problem

The pore-scale model developed in Section 2 is employed to study the multiphase reactive transport processes related to dissolution trapping during CO_2 sequestration in deep brine. The physicochemical processes under investigation are introduced as follows. Initially, scCO_2 and brine coexist in the void space of porous rocks due to capillary trapping, as schematically shown in Fig. 1(a). Then, scCO_2 dissolves into the brine through the scCO_2-brine interface, generating CO_2(aq) which exists in equilibrium with carbonic acid H_2CO_3. Subsequently, dissociation of H_2CO_3 takes place generating HCO_3^- and CO_3^{2-}. Chemical reactions related in the above processes are described by the following equations in the canonical form (See. Eq. (14))

$$CO_2(g) \leftrightarrow CO_2(aq) \tag{23-a}$$

$$H_2O + CO_2(aq) - H^+ \leftrightarrow HCO_3^- \tag{23-b}$$

$$H_2O + CO_2(aq) - 2H^+ \leftrightarrow CO_3^{2-} \tag{23-c}$$

$$H_2O - H^+ \leftrightarrow OH^- \tag{23-d}$$

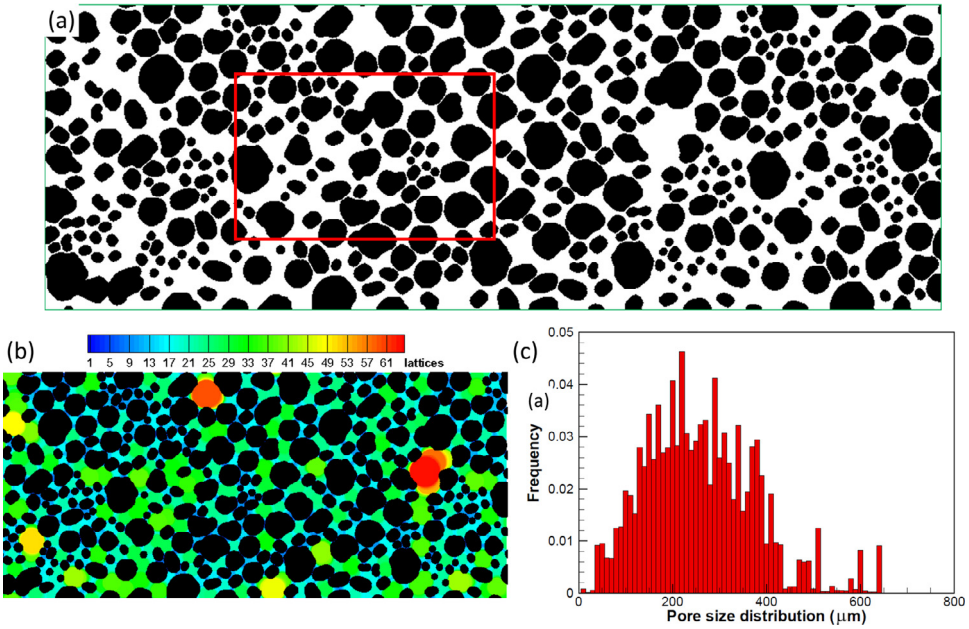

Fig. 2. The computational domain. (a) A 3000*1000 2D micromodel porous medium with size of each lattice as 10 μm, (b) Contour image of pore size determined using the skeletization method, and (c) Pore size distribution of the 2D micromodel.

From the above description can be found the complicated multiphase flow, multiple component transport, and chemical reactions. Note that in the present study, we focus on CO_2 dissolution trapping. Therefore the chemical reactions between ions in the aqueous phase and minerals in the solid rock during mineral trapping process are not considered, which will be topic of further studies. In practice, while mineral dissolution and precipitation reactions occur at some CO_2 sequestration sites, such reactions are minor at other sites (Jun et al., 2013). If such fluid-solid kinetic reactions should be considered, for example if H^+ is involved in the kinetic reactions, they can be treated in boundary conditions (Chen et al., 2015a).

To experimentally investigate pore-scale coupled flow and reactive transport process, compared with 3D micro-tomography 2D micromodel of porous media has the advantage to conduct direct observations and continuous records of the complicated multiphase flow and dissolution processes. As stated by Buchgraber et al. (2012) "*Micromodels provide the best means to visualize fluid movement at the pore scale while honoring both geometric and topologic properties of real rocks*". In fact, 2D micromodel has been adopted to investigate reactive transport processes related to CO_2 sequestration, such as wettability alternation of mineral by $scCO_2$ (Kim et al., 2012), $scCO_2$ imbibition and drainage (Zhang et al., 2011), CO_2 ex-solution (Xu et al., 2017), and dissolution and precipitation processes (Yoon et al., 2012; Kim et al., 2013).

Therefore, 2D micromodel is also adopted for numerical simulations in the present work. While such 2D simulation results cannot (and should not) be interpreted as those of an identical 2D slice from a 3D simulation, they indeed reveal some underlying physicochemical processes as will be discussed in Section 4. For real practice and applications, 3D studies are necessary, which is the object of future work. The extension of our pore-scale model from 2D to 3D is easy and straightforward. The 2D micromodel matrix used is shown in Fig. 2(a), the size of which is 3000*1000, with size of each grid as 10 μm. The 26 point labeling scheme is adopted for identifying the solid particle number and size (Chen et al., 2015b), and the skeletization method (Delerue et al., 1999) is employed to determine the pore size distribution. There are totally 428 solid particles in the domain with averaged size of about 153 μm. In skeletization method, the local pore size of any point P in the void space is defined as the radius of the largest circle which is centered in the solid skeleton and includes point P. Fig. 2(b) shows the contour image of the pore size of each node in the void space. Fig. 2(c) shows the pore size distribution (PSD) of the 2D micromodel, with the peak at around 200 μm. In the present study, without loss of generality, a 800*500 domain is randomly selected from the matrix for pore-scale simulations, as demonstrated by the red box in Fig. 2(a).

The problem under investigation is a three-phase system including solid rock, brine and $scCO_2$. Components in the aqueous phase studied include CO_2(aq), H^+, HCO_3^-, CO_3^{2-} and OH^-. In our study, first a simulation is carried out for multiphase flow without reaction until steady state, and then reaction is added. This is because the steady-state multiphase distribution may be far from the initial condition and it may be time consuming to reach the steady state. However, the subsequent multiphase flow, mass transfer, and reaction are simulated simultaneously because there is no clear separation of the time scales for these processes for the problem considered in this work. Multiphase flow distributions in different rock types were experimentally studied in the literature (Iglauer et al., 2011; Andrew et al., 2014, 2013), and it is found that typical values of residual $scCO_2$ saturation are about 0.1~0.35. Hence, $scCO_2$ saturation in the range of 0.1–0.4 is studied in the present study.

Although the pore-scale multiphase model developed in this study is applied to $scCO_2$ sequestration, it also has potential applications to multiphase reactive transport processes in other scientific and engineering problems such as fuel cells.

4. Results and discussion

In this section, coupled multiphase flow and reactive transport in the 2D microscopic porous medium are studied in detail. Diffusivity for different components is assumed to be 2.0×10^{-9} m^2/s, guaranteeing conservation of charge (Chen et al., 2015a). Density of $scCO_2$ is 628.6 kg/m^3. Pressure of $scCO_2$ is 100atm, and Henry coefficient at the $scCO_2$-water interface is 0.034 M/atm, leading to saturated concentration of CO_2(aq) as 3.4 M. Equilibrium constant for reaction 23(b-d) is 4.25×10^{-7} mol/m^3, 1.99×10^{-17} mol/m^3 and 1.0×10^{-14} mol/m^3, respectively.

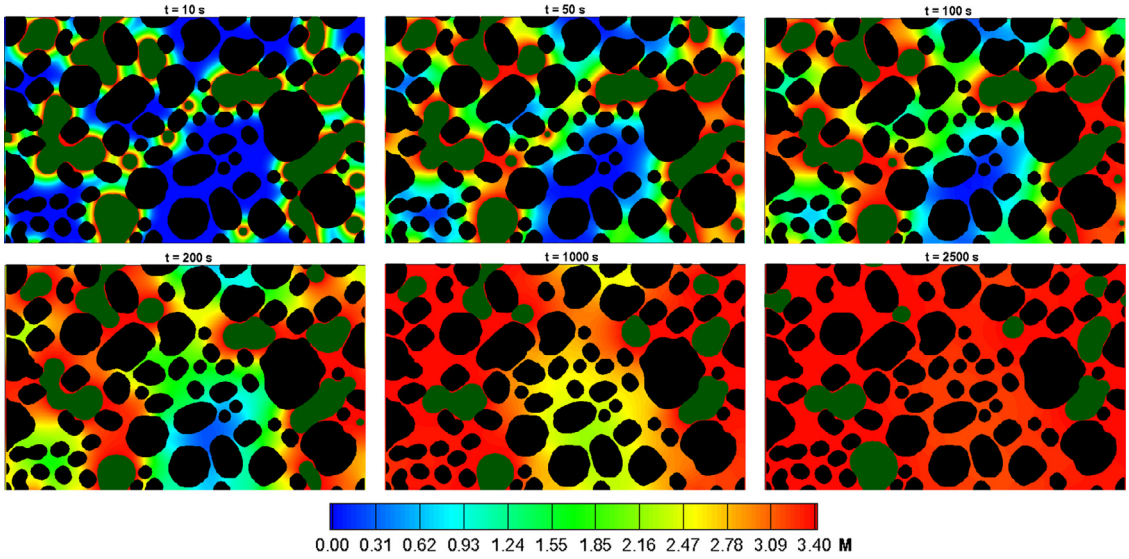

Fig. 3. Time evolutions of $scCO_2$-water two phase and CO_2(aq) concentration distribution. Initial $scCO_2$ saturation is 0.4.

4.1. Evolution of multiphase and concentration distribution

Fig. 3 shows the time evolution of $scCO_2$-water multiphase flow as well as the CO_2(aq) concentration field, where black and dark green region are solid and $scCO_2$ respectively. With an initial $scCO_2$ saturation $S_{in} = 0.4$, $scCO_2$ shows as either small clusters or individual ganglia. Initially, all the $scCO_2$ bubbles contact with fresh water, and they dissolve at relatively high rates due to local high concentration gradient, with local CO_2(aq) concentration at the liquid-gas interface quickly approaching saturated concentration of about 3.39 M. The generated CO_2(aq) then transports away from the $scCO_2$-water interface into the water with dominant mass transport mechanism as diffusion. Such diffusion mechanism is very slow, thus the dissolution reaction rate is limited by the transport rate of dissolved CO_2(aq) away from the $scCO_2$-water interface. It is also observed that in Fig. 3, the pore-scale heterogeneous multiphase and concentration distributions are obvious. Therefore, the dissolution processes of different bubbles are highly affected by local pore structures. Obviously, bubbles which are more accessible to fresh water dissolve faster. Finally, the CO_2(aq) concentration in the entire water solution reaches saturated value and the dissolution ceases at around 2500 s. Depending on bubble sizes and local porous structures, some bubbles dissolve completely while a few remain in the domain ($t = 2500$ s). From Fig. 3 it can be found that due to the limited mass transport rate, the multiphase multicomponent system is not equilibrium instantaneously, which is a dynamic process and take long time of about 2500 s to reach the equilibrium state.

The initial $scCO_2$ saturation S_{in} is reduced to 0.2 and the time evolution of the averaged CO_2(aq) concentration is shown in Fig. 4. As S_{in} reduced, CO_2(g) tends to distribute as separated small ganglia. All the $scCO_2$ can be dissolved due to more water available. The final CO_2(aq) concentration is lower than that in Fig. 3. Again, the pore-scale two-phase distribution and concentration field show high heterogeneity, and it takes about 2000s for the system to reach equilibrium state.

4.2. Evolution of saturation and averaged concentration

Fig. 5(a) and (b) shows the time evolution of the averaged CO_2(aq) concentration and $scCO_2$ saturation, respectively. The averaged CO_2(aq) concentration in the water is defined as follows

$$\overline{C_{CO_2(aq)}} = \frac{\int_{A_{water}} C_{CO_2(aq)} d_A}{A_{water}} \tag{24}$$

As shown in Fig. 5(a) for all the cases, $\overline{C_{CO_2(aq)}}$ first goes up and then reaches a constant value. For the cases with initial $scCO_2$ saturation $S_{in} = 0.4$ and 0.3, the final constant $\overline{C_{CO_2(aq)}}$ is about 3.39 M, which is the saturated concentration of dissolved CO_2(aq) under the pressure and temperature condition studied. Reaching the saturated CO_2(aq) concentration means there are sufficient CO_2(g) in the system, and thus there is $scCO_2$ remaining at the end, in agreement with the contour images in Fig. 3 as well as Fig. 5(b). Besides, the case with initial $S_{in} = 0.4$ approaches the saturated CO_2(aq) concentration at about 3000 s, much earlier than the case with $S_{in} = 0.3$ which arrives at about 9000 s. This is because higher S_{in} leads to more $scCO_2$-water interface for dissolution and limited space of aqueous phase for mass transport. Further reducing S_{in} to 0.2 and 0.1, the final $\overline{C_{CO_2(aq)}}$ is about 2.25 M and 1.06 M, respectively, lower than the saturated value indicating no residual CO_2(g) in the system as shown in Fig. 4 ($t = 1500$) and Fig. 5(b).

As shown in Fig. 5(a), for the case with initial $S_{in} = 0.2$, $\overline{C_{CO_2(aq)}}$ reaches the constant value at around 1000 s, however, a small $scCO_2$ bubble is still undergoing dissolution at $t = 1000$ s and concentration gradient still exists in the system even at $t = 1500$ s (as shown in Fig. 4). In the continuum-scale study, a constant $\overline{C_{CO_2(aq)}}$ indicates the system reaches the equilibrium stage. However, the pore-scale results here clearly demonstrate that arriving a constant $\overline{C_{CO_2(aq)}}$ does not correspond to the equilibrium stage, because pore-scale heterogeneity may still exist and pore-scale mass transport may be still proceeding.

4.3. Evolution of pH

Fig. 6(a) shows the pH value distribution at $t = 10$ s for $S_{in} = 0.4$. As expected, due to dissolution of $scCO_2$ and subsequent dissociation of H_2CO_3, pH value is reduced in the water solution. Local region with strong dissolution shows a pH value as low as about 3; while due to slow mass transport, these regions far away from dissolution regions remain the initial neutral solution, as shown in the red region in Fig. 6(a). Fig. 6(b) shows the time evolution of the averaged pH value in the water. As expected, for all the cases pH value decreases as time proceeds. For the case with $S_{in} = 0.4$ and 0.3, the final pH values are identical of about 2.9. For the complete dissolution case of $S_{in} = 0.2$ and 0.1, the final pH value increases as S_{in} decreases due to less H^+ generated. Note that in the present study, the chemical reactions between acidic solution and the hosting rock, which may lead to solid surface de-wetting, mineral dissolution, or precipitation, are not taken into account. Obviously, if such reactions are considered, H^+ will be consumed, which will fa-

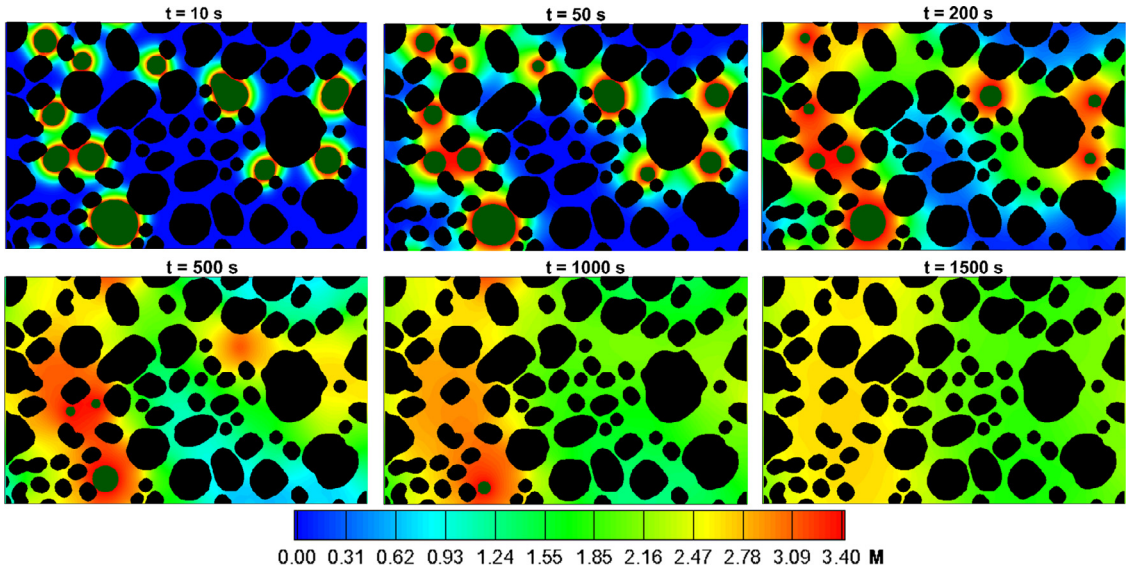

Fig. 4. Time evolutions of $scCO_2$-water two phase and CO_2(aq) concentration distribution. Initial $scCO_2$ saturation is 0.2.

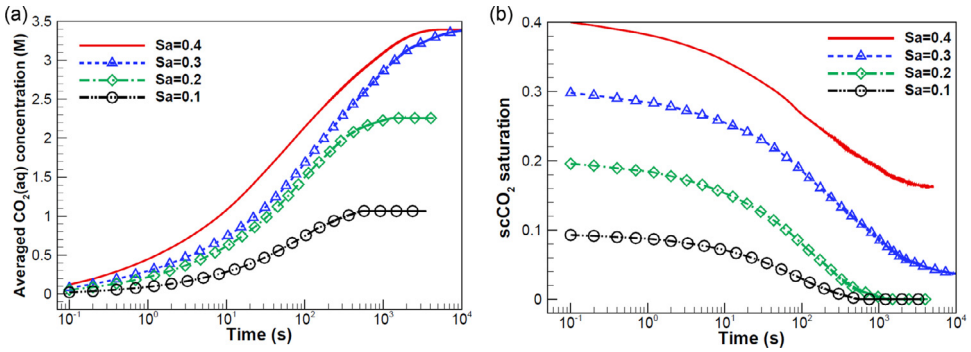

Fig. 5. Time evolution of the averaged CO_2(aq) concentration in the aqueous phase (a) and $scCO_2$ saturation (b).

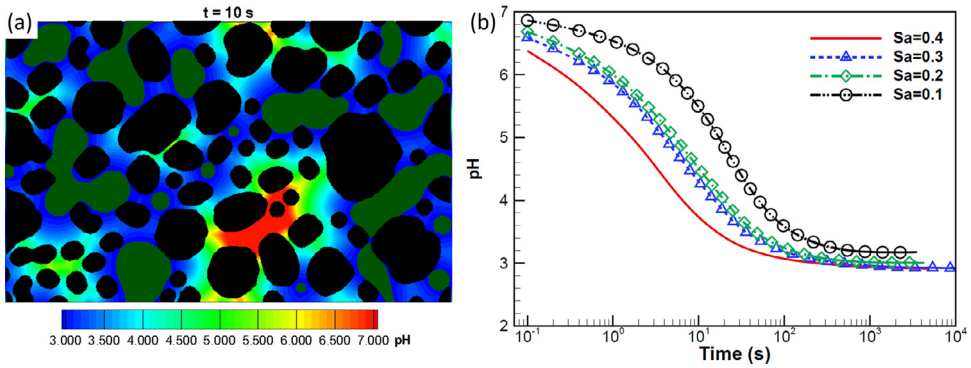

Fig. 6. pH value distribution in the domain at $t = 10$ s (a) and time evolutions of the averaged pH in the solution (b).

cilitate the $scCO_2$ dissolution. Such effects will be the topic of a further study in the future.

4.4. Evolution of interfacial length

The interfacial area between different phases in porous media has been demonstrated as a critical entity to improve understanding of multiphase flow. It has been proposed as an additional variable for multiphase flow models (Majid Hassanizadeh and Gray, 1993; Karadimitriou et al., 2014). In the coupled multiphase flow and reactive transport processes, heterogeneous chemical reaction occurs exactly at the phase interface, thus interfacial area as well as interface evolution significantly affects the reaction rate and local mass transport. For multiphase flow in porous media, there are multiple kinds of phase interfaces in the system. It should be pointed out interfacial area in 3D is reduced to interfacial length in 2D. To avoid any confusion, here the term "interfacial length" is adopted.

Taking the problem studied in this study as an example, three kinds of interface coexist in the system, namely $scCO_2$-water, water-solid and $scCO_2$-solid interface, which are denoted by A_{lg}, A_{ls} and A_{gs}, respectively. Fig. 7 shows the variation of $scCO_2$-water specific interfacial length with time during $scCO_2$ dissolution process, where the

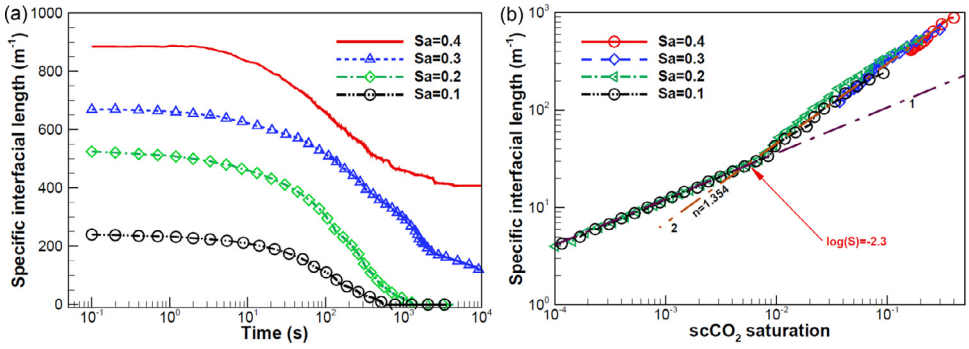

Fig. 7. Time evolution of the liquid-gas interfacial length (a) and relationship between $scCO_2$ saturation and interfacial length (b).

$scCO_2$-water specific interfacial length $\overline{A}_{lg}$ is defined as ratio between A_{lg} and the area of the entire computational domain containing both void and solid space. As shown in Fig. 7(a), for each case, $\overline{A}_{lg}$ decreases and finally reaches a final constant value as time proceeds. The cases with $S_{in}=0.4$ and 0.3 reach final value $\overline{A}_{lg}$ of about 500 m^{-1} and 200 m^{-1}, respectively; while for the cases $S_{in}=0.2$ and 0.1 the final value is zero due to complete dissolution of $scCO_2$.

In continuum models, details of pore-scale multiphase flow distributions are not resolved. Thus interfacial surface area (or interfacial length in 2D) cannot be quantitatively determined, which, however, is required for evaluating reaction flux in such models. Therefore, in continuum models empirical relationship is usually adopted to evaluate surface area based on saturation. Pore-scale studies can provide such empirical relationships. Fig. 7(b) displays the variations of $\overline{A}_{lg}$ as a function of saturation S during the dissolution processes. The most interesting result is that although pore-scale multiphase distributions and evolutions are quite complex during the dissolution processes as shown in Figs. 3 and 4, for the four cases $\log(\overline{A}_{lg})$~$\log(S)$ curves almost overlap; further, they show a linear relationship, indicating a power-law relationship between $\overline{A}_{lg}$ and S. The linear relationship shows a dual slop behavior with first part ending at about $S=0.005$ (or $\log(S)=-2.3$). In terms of application to continuum-scale modeling only the second part of the curve where $n=1.354$ is useful, as for the first part the saturation is extremely low (below 0.005). The reason for such dual slop characteristic is not clear currently. To the best of our knowledge for coupled multiphase flow and dissolution processes studied in the present study, there is no $\overline{A}_{lg} \sim S$ relationship determined from pore-scale experimental or numerical studies. There are indeed some studies in the literature to determine $\overline{A} \sim S$ relationship during drainage-imbibition processes in porous media. 2D microfluidic experiments of Zhang et al. (2011) indicate a linear relationship. Such linear relationship was later confirmed by 2D pore-scale numerical studies using LB (Liu et al., 2015). However in the work of Ref. (Zhang et al., 2011; Liu et al., 2015), there is no reaction.

4.5. Mass transport coefficient (efficient dissolution rate)

In the continuum theory of subsurface flow and mass transfer, the change in concentration is described by the following set of equations

$$\frac{\partial}{\partial t}[(1-S_g)\overline{C}] = D\left[(1-S_g)\frac{\partial^2 \overline{C}}{\partial x^2} - \frac{\partial S_g}{\partial x}\frac{\partial \overline{C}}{\partial x}\right] - \frac{u}{\varepsilon}\frac{\partial \overline{C}}{\partial x} + kA(C_S - \overline{C}) \tag{25-a}$$

$$\frac{\partial S_g}{\partial t} = -kA(C_S - \overline{C})M/\rho \tag{25-b}$$

in which M and ρ are the molar mass and density of CO_2(aq), respectively. C_S is the equilibrium or saturated concentration of CO_2(aq). k is the mass transport coefficient or the efficient dissolution reaction rate coefficient. If the whole computational domain of the present pore-scale study is considered as a unit cell (a mesh) in the continuum-scale model, the inner diffusion is not considered. Further, fully periodic boundary conditions are adopted. Thus, Eq. (25) can be reduced to the following zero-order form

$$\frac{d}{dt}[(1-S_g)\overline{C}] = kA(C_S - \overline{C}) \tag{26-a}$$

$$\frac{dS_g}{dt} = -kA(C_S - \overline{C})M/\rho \tag{26-b}$$

Note that conventionally kA is lumped together to be determined, because it is challenging to experimentally distinguish phase interface within a porous medium. Benefited from our pore-scale study in which phase interface is explicitly resolved, A can be quantitatively counted and thus k and A can be decoupled. The variations of S, $\overline{C}$ and A with time have already been shown in previous figures. Here, we rearrange these variables and plot $d[(1-S_g)\overline{C}]/dt$ and $A(C_S-\overline{C})$ along y and x axis, respectively, from which the mass transport coefficient, namely the slop of the curve, can be estimated. In this study, both the $scCO_2$ and water are almost at rest, thus the dissolution rate is controlled by the diffusion of dissolved CO_2(aq) in the water. Therefore, k is expected to decay as the CO_2(aq) concentration in the water increases, as shown by the reduced slop of the curves in Fig. 8(a). Finally, k approaches zero due to either complete $scCO_2$ dissolution or solution saturation. Gradually decreasing k during the dissolution process indicates a strong coupling between dissolution reaction and mass transport processes, and the dominated diffusion mass transport mechanism leads to a prolonged time required for the system to reach equilibrium stage. We also plot the $d[(1-S_g)\overline{C}]/dt$ vs $(C_S-\overline{C})$ in Fig. 8(b), meaning that kA is lumped together. Compared Fig. 8(a) and (b), it can be seen the trends are quite different. On the one hand, dissolution will terminate either due to saturated solution ($C_S-\overline{C}=0$) or complete dissolution ($A=0$), all the curves in Fig. 8(a) end at origin of coordinates, while in Fig. 8(b) different curves end at different locations along x axis. On the other hand, both the reactive surface area and concentration gradient affect the dissolution process. Therefore, decoupling k and A not only agrees with practical physicochemical processes but also facilitate to propose empirical relationship for k.

4.6. Effects of wettability

Wettability of a porous medium is a main factor affecting the strength of capillary force during multiphase flow. It can be measured by the contact angle created at the fluid-fluid and fluid-solid interfaces. Effects of wettability on $scCO_2$ dissolution is also investigated. Fig. 9(a) and (b) shows the two-phase distribution as well as the concentration field for contact angles of 125° and 90° at $t=10$ s. It can be seen that as $scCO_2$ contact angle decreases, $scCO_2$ changes from ganglia to strip shape, and more solid surface is covered by $scCO_2$. Fig. 9(c) shows the time evolution of $scCO_2$-water specific interfacial length $\overline{A}_{lg}$. It can be found that the higher the contact angle, the higher $\overline{A}_{lg}$. However, common sense

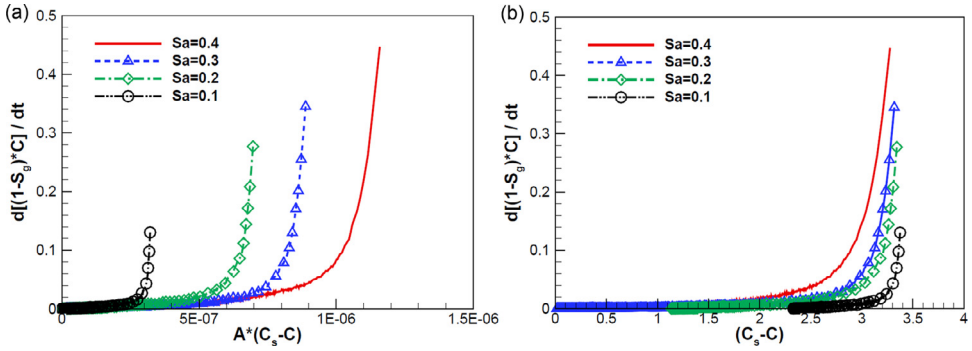

Fig. 8. Dependence of $d[(1-S_g)\overline{C}]/dt$ on $A(C_S-\overline{C})$ (a) and on $(C_S-\overline{C})$ (b).

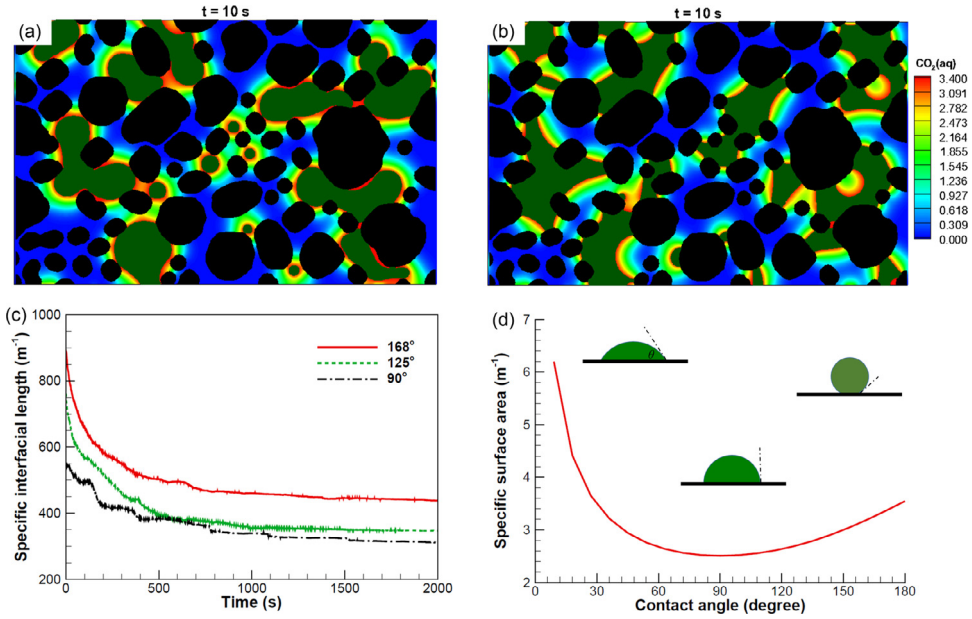

Fig. 9. Effects of wettability on $scCO_2$ dissolution. $scCO_2$-water two phase and CO_2(aq) concentration distribution for (a) contact angle of 125° and (b) contact angle of 90°. (c) Time evolution of specific interfacial length. (d) The variations of fluid-fluid interfacial length for a droplet sitting on a plate solid surface with different contact angles, in which area of different droplets is the same.

is that for spherical crowns with the same volume, the higher the contact angle is, the lower the surface area is, as the spherical crown is closer to a sphere and among different morphologies the sphere has the lowest surface area for the same volume. This is because $\overline{A}_{lg}$ discussed here is the fluid-fluid interfacial length rather than the entire interfacial length of the $scCO_2$ which contains both fluid-fluid and fluid-solid interfacial length. To illustrate this point, Fig. 9(d) further displays the variations of fluid-fluid interfacial length for a droplet sitting on a plate solid surface with different contact angles, in which area of different droplets is the same. It can be found that as the contact angle increases, the specific interfacial length first decreases and then increases, with minimum specific interfacial length at neutral wettability. The change trend in Fig. 9(d) supports the results in Fig. 9(c). Lower $scCO_2$-water surface area results in slower dissolution rate, which has been discussed in previous sections, and the results are not repeated here for brevity.

5. Conclusion

In classical continuum models, $scCO_2$ dissolution during solubility trapping has been considered to instantaneously reach equilibrium stage. However, recently experimental results show that depletion of residual $scCO_2$ is a prolonged process indicating non-equilibrium dissolution. In this study, a pore-scale numerical model for multiphase multicomponent reactive transport processes is developed and applied to study pore-scale $scCO_2$ dissolution process. The purpose of the pore-scale study is to provide details of multiphase distribution and flow, mass transport, homogeneous and heterogeneous reactions at the pore scale, and thus to gain deep understanding of the underlying multiple physiochemical transport processes and interactions among different processes. A 2D micromodel porous medium is adopted as the computational domain, whose pore size distribution and solid particle size are analyzed. Coupled processes during CO_2 solubility trapping including $scCO_2$-water two phase flow, interfacial $scCO_2$ dissolution reaction, homogeneous dissociation reactions in the bulk fluid, and multicomponent transport (CO_2(aq), H^+, HCO_3^-, CO_3^{2-} and OH^-) are simulated within the 2D micromodel. Time evolutions of multiphase and concentration distributions are provided and discussed. Variations of saturation, averaged concentration, specific interfacial length, pH value are also analyzed. The conclusions are summarized as follows:

(1) It is found that non-uniform distribution of $scCO_2$ and slow mass transport of generated components away from the reactive interface lead to prolonged $scCO_2$ dissolution processes. The dissolution of a $scCO_2$ ganglion greatly depends on local pore structures and multiphase distributions. For the 8 mm × 5 mm 2D domain studied in this study, it usually takes thousands of seconds to

reach the final equilibrium stage, indicating a typical transport-controlled non-equilibrium dissolution process.

(2) While a constant averaged concentration in the domain is an indicator of equilibrium state in the continuum model, it is not the case at the pore scale, because pore-scale heterogeneity still exists and local transport still proceeds.

(3) Benefited from directly resolved pore-scale multiphase distribution, interfacial length can be quantitatively determined. For the cases studied in the present study, a power-law relationship is predicted between saturation and interfacial surface area during the dissolution processes.

(4) Mass transport coefficient or effective dissolution rate k is calculated and it is found that k decreases as dissolution proceeds due to gradually saturated solution.

(5) For $scCO_2$ contact angle above 90°, it is found that as contact angle increases, the dissolution rate also increases, this is because dissolution reaction occurs only at fluid-fluid interface rather than the entire phase interface including both fluid-fluid and fluid-solid interface.

Finally, we want to point out that many multiphase reactive transport processes, such as CO2 sequestration is actually a multiscale process. The key difficulty for studying such multiscale process is the large variability of the characteristic length and time scales of the reactive transport processes. While continuum-scale studies are performed at the large-scale of engineering interest, the flow, mass transport, and chemical reactions actually take place at the microscopic regions in local regions such as phase interface and pores within the porous medium. Therefore there is a “scale disparity” for adopting continuum models to describe reactive transport in porous medium. Pore-scale studies, not only help to understand the underlying transport features and to investigate effects of important factors such as porous structures and surface wettability, but also can provide physics-based relationships to close the continuum models, such as the saturation-surface area in the present study and other relationships such as porosity-permeability (or relative permeability). Unfortunately, currently these relationships are only available for porous media with relatively simple geometries. Therefore, in future studies, we will further apply our pore-scale multiphase multicomponent reactive transport model to reveal effects of operating and structural parameters, and to upscale our pore-scale results to improve continuum models.

Acknowledgment

Li Chen thanks the support of National Nature Science Foundation of China (51776159), Innovative Talents Support Plan of China Postdoctoral Foundation and the Fundamental Research Funds for the Central Universities. Qinjun Kang acknowledges the support of LANL’s LDRD Program and Institutional Computing Program. The authors thank Mark Porter for providing the pore structure of the 2D micromodel used in this study.

Supplementary materials

Supplementary material associated with this article can be found, in the online version, at doi:10.1016/j.advwatres.2018.02.018.

References

Akbarabadi, M., Piri, M., 2013. Relative permeability hysteresis and capillary trapping characteristics of supercritical CO2/brine systems: an experimental study at reservoir conditions. Adv. Water Res. 52, 190–206.

Andrew, M., Bijeljic, B., Blunt, M.J., 2013. Pore-scale imaging of geological carbon dioxide storage under in situ conditions. Geophys. Res. Lett. 40 (15), 3915–3918.

Andrew, M., Bijeljic, B., Blunt, M.J., 2014. Pore-scale imaging of trapped supercritical carbon dioxide in sandstones and carbonates. Int. J. Greenhouse Gas Control 22, 1–14.

Buchgraber, M., Kovscek, A.R., Castanier, L.M., 2012. A Study of microscale gas trapping using etched silicon micromodels. Transp. Porous Media 95 (3), 647–668.

Chang, C., Zhou, Q., Kneafsey, T.J., Oostrom, M., Wietsma, T.W., Yu, Q., 2016. Pore-scale supercritical CO2 dissolution and mass transfer under imbibition conditions. Adv. Water Res. 92, 142–158.

Chang, C., Zhou, Q., Oostrom, M., Kneafsey, T.J., Mehta, H., 2017. Pore-scale supercritical CO2 dissolution and mass transfer under drainage conditions. Adv. Water Res. 100, 14–25.

Chaudhary, K., Cardenas, M.B., Wolfe, W.W., Maisano, J.A., Ketcham, R.A., Bennett, P.C., 2013. Pore-scale trapping of supercritical CO2 and the role of grain wettability and shape. Geophys. Res. Lett. 40 (15), 3878–3882.

Chen, L., Feng, Y.-L., Song, C.-X., Chen, L., He, Y.-L., Tao, W.-Q., 2013a. Multi-scale modeling of proton exchange membrane fuel cell by coupling finite volume method and lattice Boltzmann method. Int. J. Heat Mass Transfer 63, 268–283.

Chen, L., Kang, Q., Mu, Y., He, Y.-L., Tao, W.-Q., 2014. A critical review of the pseudopotential multiphase lattice Boltzmann model: methods and applications. Int. J. Heat Mass. Transfer 76 (0), 210–236.

Chen, L., Kang, Q., Robinson, B.A., He, Y.-L., Tao, W.-Q., 2013b. Pore-scale modeling of multiphase reactive transport with phase transitions and dissolution-precipitation processes in closed systems. Phys. Rev. E 87 (4), 043306.

Chen, L., Kang, Q., Tang, Q., Robinson, B.A., He, Y.-L., Tao, W.-Q., 2015a. Pore-scale simulation of multicomponent multiphase reactive transport with dissolution and precipitation. Int. J. Heat Mass Transfer 85 (Suppl C), 935–949.

Chen, L., Luan, H.-B., He, Y.-L., Tao, W.-Q., 2012. Pore-scale flow and mass transport in gas diffusion layer of proton exchange membrane fuel cell with interdigitated flow fields. Int. J. Therm. Sci. 51 (Suppl C), 132–144.

Chen, L., Wu, G., Holby, E.F., Zelenay, P., Tao, W.-Q., Kang, Q., 2015b. Lattice Boltzmann pore-scale investigation of coupled physical-electrochemical processes in C/Pt and non-precious metal cathode catalyst layers in proton exchange membrane fuel cells. Electrochim. Acta 158, 175–186.

Chen, S.Y., Doolen, G.D., 1998. Lattice Boltzmann method for fluid flows. Ann. Rev. Fluid Mech. 30, 329–364.

Delerue, J.F., Perrier, E., Yu, Z.Y., Velde, B., 1999. New algorithms in 3D image analysis and their application to the measurement of a spatialized pore size distribution in soils. Phys. Chem. Earth Part A 24 (7), 639–644.

Huber, C., Parmigiani, A., Chopard, B., Bachmann, O., 2011. Pore-scale mass and reactant transport in multiphase porous media flows. J. Fluid Mech. 686 (40), 1–37.

Iglauer, S., Paluszny, A., Pentland, C.H., Blunt, M.J., 2011. Residual CO2 imaged with X-ray micro-tomography. Geophys. Res. Lett. 38 (21), L049680.

IPCC, 2005. IPCC Special Report on Carbon Dioxide Capture and Storage. Cambridge University Press, Cambridge.

Jun, Y.-S., Giammar, D.E., Werth, C.J., 2013. Impacts of geochemical reactions on geologic carbon sequestration. Environ. Sci. Technol. 47 (1), 3–8.

Kang, Q., Lichtner, P., Viswanathan, H., Abdel-Fattah, A., 2010. Pore scale modeling of reactive transport involved in geologic CO_2 sequestration. Transp. Porous Media 82 (1), 197–213.

Kang, Q., Lichtner, P.C., Zhang, D., 2006. Lattice Boltzmann pore-scale model for multicomponent reactive transport in porous media. J. Geophys. Res. 111 (B5) n/a-n/a.

Kang, Q., Zhang, D., Chen, S., He, X., 2002. Lattice Boltzmann simulation of chemical dissolution in porous media. Phys. Rev. E 65 (3), 036318.

Karadimitriou, N.K., Hassanizadeh, S.M., Joekar-Niasar, V., Kleingeld, P.J., 2014. Micromodel study of two-phase flow under transient conditions: Quantifying effects of specific interfacial area. Water Resour. Res. 50 (10), 8125–8140.

Kim, M., Sell, A., Sinton, D., 2013. Aquifer-on-a-chip: understanding pore-scale salt precipitation dynamics during CO2 sequestration. Lab Chip 13, 2508–2518.

Kim, Y., Wan, J., Kneafsey, T.J., Tokunaga, T.K., 2012. Dewetting of silica surfaces upon reactions with supercritical CO2 and brine: pore-scale studies in micromodels. Environ. Sci. Technol. 46 (7), 4228–4235.

Kupershtokh, A.L., Medvedev, D.A., Karpov, D.I., 2009. On equations of state in a lattice Boltzmann method. Comput. Math. Appl. 58 (5), 965–974.

Liu, H., Zhang, Y., Valocchi, A.J., 2015. Lattice Boltzmann simulation of immiscible fluid displacement in porous media: homogeneous versus heterogeneous pore network. Phys. Fluids 27, 052103.

Luquot, L., Gouze, P., 2009. Experimental determination of porosity and permeability changes induced by injection of CO2 into carbonate rocks. Chem. Geol. 265 (1–2), 148–159.

Majid Hassanizadeh, S., Gray, W.G., 1993. Thermodynamic basis of capillary pressure in porous media. Water Resour. Res. 29 (10), 3389–3405.

Noiriel, C., Luquot, L., Madé, B., Raimbault, L., Gouze, P., van der Lee, J., 2009. Changes in reactive surface area during limestone dissolution: an experimental and modelling study. Chem. Geol. 265 (1–2), 160–170.

Paterson, L., Boreham, C., Bunch, M., Dance, T., Ennis-King, J., Freifeld, B., Haese, R., Jenkins, C., LaForce, T., Raab, M., Singh, R., Stalker, L., Zhang, Y., 2013. Overview of the CO2CRC otway residual saturation and dissolution test. Energy Procedia 37, 6140–6148.

Pentland, C.H., El-Maghraby, R., Iglauer, S., Blunt, M.J., 2011. Measurements of the capillary trapping of super-critical carbon dioxide in Berea sandstone. Geophys. Res. Lett. 38 (6), L06401.

Porter, M.L., Coon, E.T., Kang, Q., Moulton, J.D., Carey, J.W., 2012. Multicomponent interparticle-potential lattice Boltzmann model for fluids with large viscosity ratios. Phys. Rev. E 86 (3), 036701.

Shan, X., Chen, H., 1993. Lattice Boltzmann model for simulating flows with multiple phases and components. Phys. Rev. E 47, 1815–1819.

Soltanian, M.R., Amooie, M.A., Gershenzon, N., Dai, Z., Ritzi, R., Xiong, F., Cole, D.R., Moortgat, J., 2017. Dissolution trapping of carbon dioxide in heterogeneous aquifers. Environ. Sci. Technol. 51 (13), 7732–7741.

Szymczak, P., Ladd, A.J.C., 2009. Wormhole formation in dissolving fractures. J. Geophys. Res. 114 (B6), B06203.

Tartakovsky, A.M., Meakin, P., Scheibe, T.D., Eichler West, R.M., 2007. Simulations of reactive transport and precipitation with smoothed particle hydrodynamics. J. Comput. Phys. 222 (2), 654–672.
Xu, R., Li, R., Huang, F., Jiang, P., 2017. Pore-scale visualization on a depressurization-induced CO2 exsolution. Sci. Bull. 62 (11), 795–803.
Yoon, H., Valocchi, A.J., Werth, C.J., Dewers, T., 2012. Pore-scale simulation of mixing-induced calcium carbonate precipitation and dissolution in a microfluidic pore network. Water Resour. Res. 48 (2), W02524.
Zhang, C., Oostrom, M., Grate, J.W., Wietsma, T.W., Warner, M.G., 2011. Liquid CO2 displacement of water in a dual-permeability pore network micromodel. Environ. Sci. Technol. 45 (17), 7581–7588.
Zhang, J., 2011. Lattice Boltzmann method for microfluidics: models and applications. Microfluid. Nanofluid. 10 (1), 1–28.
Zhang, T., Shi, B., Guo, Z., Chai, Z., Lu, J., 2012. General bounce-back scheme for concentration boundary condition in the lattice-Boltzmann method. Phys. Rev. E 85 (1), 016701.